Fine-tuning the Electrocatalytic Regeneration of NADH Cofactor using [Rh(Cp*)(bpy)Cl] + Functionalized Metal-Organic Framework Films

Weiwei Li, Chunhua Zhang, Ziman Zheng, Xiaoyu Zhang, Lin Zhang, Alexander Kuhn

Fine-tuning the Electrocatalytic Regeneration of NADH Cofactor using $[Rh(Cp^*)(bpy)Cl]^+$ Functionalized Metal-Organic Framework Films

Weiwei Li,[†‡] Chunhua Zhang,[†‡] Ziman Zheng,[†] Xiaoyu Zhang,[†] Lin Zhang,[†] Alexander Kuhn[†#*]*

† Engineering Research Center for Nanomaterials, Henan University, Kaifeng, 475000, China.

University Bordeaux, CNRS, Bordeaux INP, ISM UMR 5255, Site ENSCBP, Pessac, 33400, France.

KEYWORDS: NU-1000 film, electroenzymatic synthesis, electrocatalysis, redox hopping, NADH regeneration.

ABSTRACT

Electrochemical regeneration of the reduced form of the nicotinamide adenine dinucleotide (NADH) cofactor catalyzed by immobilized $[Rh(Cp^*)(bpy)Cl]^+$ is a promising approach for enzymatic synthesis of many valuable chemicals with NAD-dependent dehydrogenases. However, a rational control of the efficiency is often limited by the irregular structure of the electrode/electrolyte interface and the accessibility of the molecular catalyst. Here, we propose an electrochemical system for NADH cofactor regeneration, based on highly ordered 3D metal-organic framework (NU-1000) films. $[Rh(Cp^*)(bpy)Cl]^+$ is incorporated at the zirconium nodes of NU-1000 via solvent-assisted ligand incorporation (SALI), leading to a diffusion-controlled behavior, associated with an electron hopping mechanism. Varying the ratio of redox-active $[Rh(Cp^*)(bpy)Cl]^+$ and inactive post-grafting agents enables the elaboration of functional electrodes with tunable electrocatalytic activity for NADH regeneration. The exceptionally high Faradaic efficiency of 97%, associated with a very high turnover frequency (TOF) of ~1400 h^{-1} for NADH regeneration, and the total turnover number (TTN) of over 20000 for the enzymatic conversion from pyruvate to L-lactate, when coupled with L-Lactate dehydrogenases (LDH) as a model reaction, open up promising perspectives for employing these electrodes in various alternative bioelectrosynthesis approaches.

INTRODUCTION

Oxidoreductases have been widely used for bio-transformations due to their high activity and enantioselectivity under mild operating conditions. The regeneration of the reduced form of the nicotinamide adenine dinucleotide (NADH) cofactor is of great interest for potential industrial applications of enzymatic synthesis, due to the fact that around 80% of known oxidoreductases are nicotinamide dinucleotide (NAD) dependent enzymes. However, the expensive NADH cofactor is a crucial ingredient, since it directly participates in the enzymatic redox reactions.[1] Thus, over the last decades, the regeneration of NADH has been intensively investigated by enzymatic, chemical, photochemical, [2,3] and electrochemical methods.[4] The electrochemical regeneration of NADH can be considered as an attractive concept, since electricity can originate from sustainable resources and therefore enables in principle a green chemistry approach with low cost. However, the direct electrochemical reduction of NAD needs rather high overpotentials, leading to the formation of biologically inactive NAD_2 dimers or isomers instead of the active 1,4-NADH in a two–step reaction mechanism.[5] In order to obtain 1,4-NADH, different electrocatalytic systems were proposed and established.[4] Among them, the organometallic catalyst $[Rh(Cp^*)(bpy)Cl]^+$ belongs to the most efficient ones and has been immobilized on electrodes, not only to increase the reusability of the catalyst, but also to prevent undesirable interactions between the functional groups of enzymes and $[Rh(Cp^*)(bpy)Cl]^+$.[6] The rhodium functionalized electrodes have been prepared, among others, by depositing polymers bearing Rh moieties,[7] or using π-π stacking interactions with carbon materials,[8] as well as through the covalent immobilization of Rh catalysts on the electrode surfaces.[9–12] Efficient NADH regeneration rates were obtained, but due to the irregular porosity of the final electrode layer (CNTs, polymers) and an uncontrolled position of the molecular catalyst units after

immobilization via adsorption, encapsulation or diazonium grafting, it is difficult to predict and fine-tune the efficiency of the electrode. Thus, a rational design of the porous structure and a precise control of catalyst loading is highly desirable for the development of efficient functional bioelectrodes. Different types of metal−organic framework materials with porous crystalline structures were explored for a variety of potential applications[13,14], including in the field of electrochemistry.[15–19]

NU-1000 is a zirconium-based metal-organic framework with a modular porous structure, which can be tailored by different functional groups.[20] Its high surface area and good stability in the aqueous phase makes it a good candidate as a support for catalyst immobilization in bio-systems. NU-1000 or its derivatives have been used for the encapsulation of enzymes such as cutinases,[21] cytochrome c,[22,23] and formate dehydrogenase,[24] leading to enhanced stability and catalytic response. The immobilization of NU-1000 metal-organic framework films on electrodes has been proposed and studied in the field of electroanalysis,[25,26] electrocatalysis[27,28] and energy storage.[29] Since the initial NU-1000 is an insulator, the electron transfer through NU-1000 films can be in general improved by following two approaches. The first option is to incorporate a conductive material into the pores of MOFs (conductive guests,[30] C_{60},[31] conducting polymers,[32] etc.). The second elegant way is to functionalize the MOF nodes or linkers with redox active moieties allowing redox hopping of charges.[33–36] When comparing the electrical conductivity of an initial NU-1000 film along different axes of the network, three orders of magnitude higher hopping coefficients are measured when the orientation of the MOF crystal is perpendicular to the electrode surface compared to a parallel alignement.[37] Therefore, it is essential to control the orientation of NU-1000 crystals on the conductive substrates. The presence of carboxyl groups on the substrate has been used for controlling the orientation of MOFs. Different substrates (Si,

Ti[38], Au[39,40,] and FTO[41,42]) have been modified with carboxyl groups before growing a NU-1000 layer, leading to a preferential perpendicular growth. Among all possible flat electrode materials, glassy carbon (GC) is one of the most suitable for the electrochemical regeneration of NADH, due to its stability and wide potential window, but the poor adhesion of films limits its application as a support. However, molecular surface functionalization can be used as an efficient strategy to improve the adhesion of films on GC.[43] Therefore, the introduction of carboxyl groups on a GC surface will not only help orientating the film growth, but also act as a stabilizing element with respect to the adhesion of a NU-1000 film. In addition, the functionalization strategy can be extended to macroporous carbon for further applications in biosynthesis.

Based on these considerations, we propose here to establish a bioelectrochemical system for the regeneration of NADH, catalyzed by a NU-1000 film grown on glassy carbon (GC) as shown in **Scheme 1.**

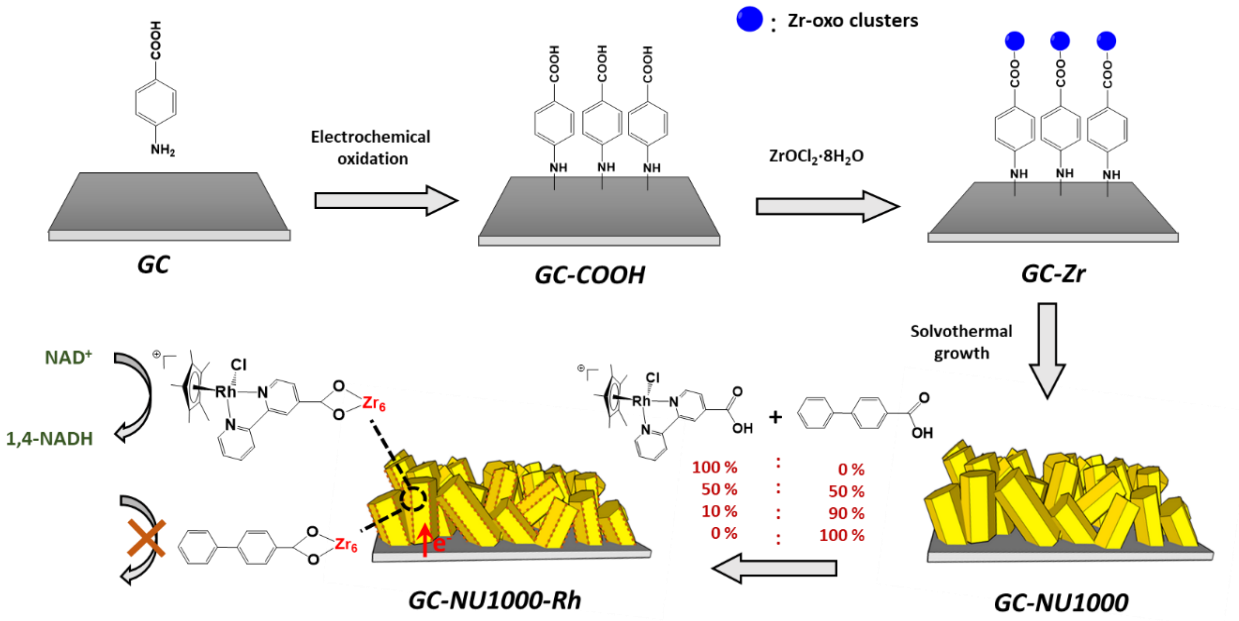

Scheme 1. Schematic illustration of the elaboration process of a $[Rh(Cp^*)(bpy)Cl]^+$ functionalized NU-1000 film on a glassy carbon electrode.

GC was first functionalized with carboxyl groups by electrooxidation of 4-aminobenzoic acid (GC-COOH). Then the formation of a NU-1000 film was triggered by a coordination step with a Zr-oxo cluster (GC-Zr), followed by a solvothermal synthesis step in precursor solution (GC-NU1000). The resulting NU-1000 film serves as a 3D framework with regularly positioned nodes, acting as a catalyst loading points. The carboxyl-functionalized Rh catalyst (Rh-COOH) can then be anchored onto the nodes of the film by solvent-assisted ligand incorporation (SALI). Taking advantage of the MOF structure, we expect to achieve the rational incorporation of a predefined amount of Rh, leading to a tunable efficiency for cofactor regeneration. The $[Rh(Cp^*)(bpy)Cl]^+$ loading of the film can be tuned and characterized by changing the initial

concentration ratio between the redox-active Rh-COOH and the redox-inactive biphenyl-4-carboxylic acid during the SALI process. The electrocatalytic performance of the resulting surface layer towards NADH regeneration can then be characterized in terms of Faradic efficiency and turnover frequency of the total system. Finally, this electrode can be applied for the electroenzymatic conversion from pyruvate to L-lactate, in the presence of L-Lactate dehydrogenases as a model enzyme.

EXPERIMENTAL METHODS

Reagents and materials

Tris (hydroxymethyl) aminomethane hydrochloride ((Tris-HCl), 99%, Macklin); β-Nicotinamide adenine dinucleotide ((β-NAD^+), ≥97%, Aladdin); β-Nicotinamide adenine dinucleotide, reduced disodium salt hydrate ((β-NADH), ≥97%, Aladdin); alcohol dehydrogenase from Saccharomyces cerevisiae (≥300 U/mg, Sigma-Aldrich); L-lactate dehydrogenase (LDH, ≥200 U/mg, Sigma-Aldrich); Sodium pyruvate (98%, Aladdin); Sodium lactate (98%, Aladdin); 1,3,6,8-tetrakis (p-benzoic acid) pyrene ((H_4TBAPy)(98%, Energy Chemical); biphenyl-4-carboxylic acid (98%, Energy Chemical); zirconium (IV) oxychloride octahydrate (99%, Energy Chemical); ferrocene (98%, Sigma-Aldrich); pentamethylcyclo-pentadienylrhodium (III) chloride dimer ($(RhCp^*Cl_2)_2$, ≥ 97%, Sigma-Aldrich); 2,2'-bipyridine-4-carboxylic acid (98%, Macklin); acetone (AR, Sinopharm); N,N-dimethylformamide ((DMF), AR, Kermel); tetrabutylammonium hexafluorophosphate (($TBAPF_6$) 98%, Sigma); 4-aminobenzoic acid (99%, Sigma); acetonitrile (AR, Macklin); methanol (AR, Tianjin Fuyu), silver nitrate (AR, Sinopharm reagent); tetrabutylammonium tetrafluoroborate ((TBAFB), 98%,

Aladdin,); acetaldehyde (AR, Sinopharm); potassium ferricyanide (99.5%, Tianjin guangfu); Glassy carbon electrodes were purchased from Tianjin aida.

Apparatus

The morphology and the energy dispersive X-ray spectroscopy (EDS) of the sample was characterized by a Field Emission Scanning Electron Microscope (GeminiSEM-500 Zeiss), and a Scanning Transmission Electron Microscopy (STEM, JEM-F200, JEOL, Akishima, Japan). The X-ray photoelectron spectroscopy (XPS) was performed with a PerkinElmer PHI 5000. The Ultraviolet − visible (UV − vis) spectra were obtained using a UV-2600 spectrophotometer (Shimadzu, Japan). The powder X-ray diffraction (PXRD) was carried out with a DX-2700BH (Cu Kα, λ = 1.5418 Å). BET adsorption was measured with a high precision gas/vapor adsorption measurement instrument (BELSORP-max Ⅱ) and the pore size measurement was carried out by using the instrument's inbuilt nonlocal density functional theory (NLDFT) model. The ultrathin section was obtained with a Leica EM UC7 Ultramicrotome. High performance liquid chromatography (HPLC) was carried out with an Agilent 1260 Infinit. The column was a Hi-plex H (7.7 × 300 mm, particle size is 8 μm).

All electrochemical experiments were carried out using an Autolab PGSTAT302N. Ag/AgCl (3.5 M KCl) and Ag^+/Ag (0.01 M $AgNO_3$ in 0.1 M TBAFB acetonitrile) were used as reference electrodes in the aqueous and organic phase, respectively. A Pt wire was used as the counter electrode.

Preparation of GC-NU1000

The glassy carbon (GC) electrode was polished with 1000 mesh sandpaper and then washed in deionized water under ultrasonication for 30 s. Then carboxyl (-COOH) groups

were generated on the GC electrode by electrochemical oxidation of 1 mM 4-aminobenzoic acid in acetonitrile. The electrochemical oxidation was conducted by running 20 cycles of cyclic voltammograms (CVs) ranging from 0 V to 1.6 V at a scan rate of 100 mV s^{-1}. Then the GC-COOH electrode was washed under ultrasonication with deionized water and ethanol. Finally, the electrode was dried for further use. After dissolving $ZrOCl_2$•$8H_2O$ (0.1 g) in 10 mL DMF the GC-COOH electrode was vertically placed in the solution and heating at 80°C in the oven for 1 h. After taking it out from the solution, the electrode was washed with DMF under ultrasonication. The film growth was carried out following a literature report .[44] 0.39 g $ZrOCl_2$• $8H_2O$ and 17.57 g biphenyl-4-carboxylic acid were dissolved in 32 mL DMF in a 100 mL round bottom flask. The solution was incubated at 80°C for 1 h and then cooled down to room temperature. Subsequently, 150 mg of 1, 3, 6, 8-tetrakis (p-benzoic acid) pyrene (H_4TBAPy) was dissolved in 30 mL of the above solution. The in-situ growth of the NU1000 film on the GC electrode (GC-NU1000) occurred by placing the GC-Zr electrode vertically in the above prepared solution. The bottle was incubated in an oil bath at 100°C for 24 h. Then the modifier biphenyl-4-carboxylic acid was removed by soaking the GC-NU1000 electrode in a solution, prepared by adding 0.5 mL 8 M HCl to 12 mL DMF at 100°C in the oven for 48 h under shaking. Finally, the electrode was soaked in acetone for 12 h in order to remove residual solvent.

Functionalization of GC-NU1000 with Rh catalyst

Carboxyl functionalized $[Rh(Cp^*)(bpy)Cl]^+$ (Rh-COOH) was immobilized at the nodes of the NU-1000 film via solvent-assisted ligand incorporation (SALI) following a literature report. [45] The solutions were prepared by mixing different ratios (0%, 10%,

50%, and 100%) of Rh-COOH with biphenyl-4-carboxylic acid. The total molar concentration of Rh-complex and biphenyl-4-carboxylic acid was kept constant for all experiments at a value of 2 mM, and the mixture was dissolved in 10 ml DMF. The SALI process was induced by dipping the GC-NU1000 electrode in the solution at 60 °C for 24 h under stirring. The obtained GC-NU1000-Rh electrodes were rinsed with acetone.

RESULTS AND DISCUSSIONS

NU-1000 films have been grown on GC via a sequence of several steps. As indicated above, the first step consists in the covalent grafting of a carboxyphenyl group, followed by the complexation with a Zr-oxo unit. The accomplishment is supported by XPS measurements. As shown in Figure 1A, the high-resolution C 1s spectra display characteristics peaks at 288.6, 287.0, 285.4 eV, corresponding to the O-C=O, C=O and C-OH functions of the carboxyl group,[43] and the peak at 284.8 eV can be attributed to the glassy carbon substrate.

The relative increase of the characteristic peak at 288.6 eV, compared to bare GC, indicates the successful attachment of the carboxyphenyl groups to the surface of the GC-COOH electrode. The Zr 3d spectra of the GC-Zr electrode exhibits two peaks at 185.5 eV and 183.1 eV, which can be assigned to Zr $3d_{3/2}$ and Zr $3d_{5/2}$, suggesting that the Zr-oxo clusters are immobilized through a reaction with the carboxyl groups. The electrochemical characteristics of the electrodes after carboxyphenyl modification were also tested by performing cyclic voltammetry with two kinds of electrochemical probes (Figure S1). The redox peaks of the negatively charged probe $Fe(CN)_6^{3-}$ almost completely disappear after carboxyphenyl functionalization due to electrostatic repulsion, while the redox peaks are identical before and after grafting of the molecular layer when ferrocene is used as a neutral probe. This indicates that the functional layer is present on

the GC electrode, but also, and most importantly, that the electron transfer is not inhibited by its presence.

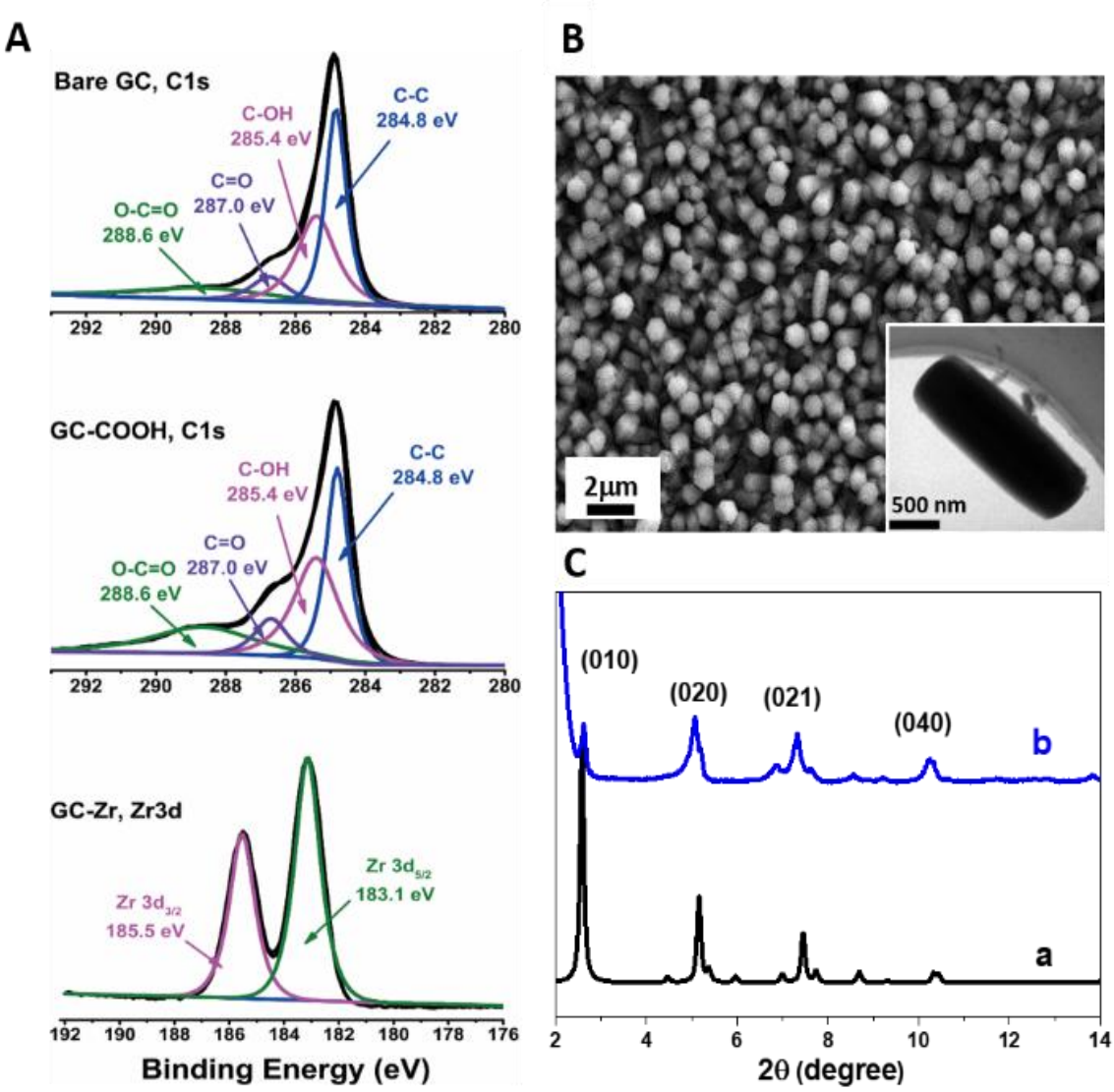

Figure 1. (A) XPS spectra of the C 1s signal for bare GC and the modified GC-COOH electrode, as well as the Zr 3d signal for the GC-Zr electrode. (B) Top view SEM image of the modified GC-NU1000 electrode. Inset: a single rod. (C) PXRD patterns of (a) simulated and (b) synthesized NU-1000. The simulated XRD data have been taken from the literature. [54]

The surfaces, pre-conditioned in this way, were then employed to grow crystalline rods of NU-1000, resulting in a film with a uniform coverage on the electrode. Figure 1B depicts SEM images of the obtained NU-1000 film, indicating that most of the crystals are growing in a perpendicular orientation to the electrode surface, and the length of individual rods is around 2~3 μm, as shown in the inset of Figure 1B. An optical picture of a representative GC-NU1000 electrode is shown in Figure S2A, illustrating again the overall homogeneity of the sample. In an important control experiment, a NU-1000 film has been grown on a bare GC electrode without carboxyphenyl functionalization. Figure S2B shows that in this case the NU-1000 film does not grow in a dense and uniform way. Unfortunately it is not possible to gradually tune the density and orientation of the MOF growth on the electrode by changing the density of the carboxyphenyl layer. Either there is a full layer or no layer at all, so fine-tuning is not possible based on this parameter. However, fine-tuning can be achieved by varying the degree of Rh loading of the MOF for a well-oriented GC-NU1000 electrode with already optimum crystal density and orientation. Thus, the very limited electrocatalytic response towards NAD^+ reduction of the control electrode prepared by catalyst crystal growth without carboxyphenyl layer, as illustrated in Figure S2C, indicates that the density and orientation of the MOF crystals severely affect the catalytic performances. The XRD spectrum recorded for the grown NU-1000 film (Figure 1C) exhibits 4 peaks corresponding to the (010), (020), (021), and (040) crystal planes and fits well with the simulated spectrum. This provides further evidence that the NU-1000 film has been successfully generated on the GC surface.

The generated NU-1000 film plays the role of a host matrix for the immobilization of the actual Rh catalyst, and it is important to control its loading in order to tune both the conductivity and the electrocatalytic performance of the film. The strategy we used in this work for the

catalyst fixation is based on solvent-assisted ligand incorporation (SALI). Carboxyl-

$[Rh(Cp^*)(bpy)Cl]^+$ was incorporated at the Zr_6 nodes of the as-prepared NU1000 film by

following this approach, and the presence of Rh catalyst was also confirmed by XPS (**Figure**

S3). In a literature report about immobilization of ferrocenecarboxylic acid in MOF powder by

the SALI approach, the ratio of ferrocene to Zr_6 has been approximately 1:1.[46] In order to control

the concentration of anchored Rh catalyst, we varied in our experiments the molar ratio of redox-

active Rh-COOH to inactive biphenyl-4-carboxylic acid during the SALI process. The obtained

GC-NU1000-Rh films with different Rh catalyst concentrations were characterized by energy

dispersive X-ray spectroscopy (EDS). The different molar percentage (0%, 10%, 50%, and

100%) of the redox-active $[Rh(Cp^*)(bpy)Cl]^+$ with respect to biphenyl-4-carboxylic acid lead to

a final molar ratio of 0.10, 0.58, and 0.91 for Rh_{atom}/Zr_{node} (Table S1), indicating that the surface concentration of the Rh catalyst follows the trend of its initial molar ratio with respect to the redox-inactive post-grafting agent, and more than 80% of the Zr_6 nodes can be in principle post-functionalized with Rh-COOH. In order to confirm the distribution of the Rh catalyst inside the crystalline NU1000 rods, the NU1000 powder collected from the electrode was covered with resin and cut into thin sections. The cross-section of the NU-1000-Rh was observed by TEM, as shown in Figure 2A. Rh is homogeneously distributed, indicating that the Rh catalyst can be attached to the host matrix by post-functionalization, even inside the NU-1000 crystalline rods. The presence of Rh catalyst inside the pores of NU-1000 was further confirmed by BET analysis (Figure 2B), because the total available surface area decreases from 2132 $m^2 \cdot g^{-1}$ to 1917 $m^2 \cdot g^{-1}$,

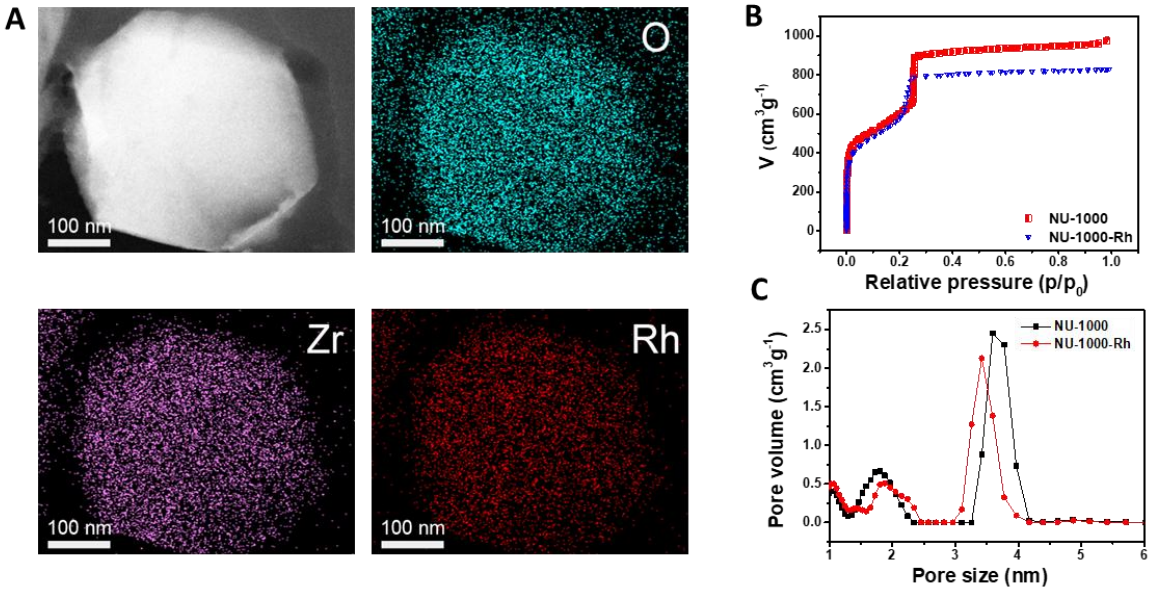

Figure 2. (A) TEM elemental mapping of the cross-section of a NU1000 crystal rod surrounded by Spurr resin. (B) The nitrogen adsorption-desorption isotherm of NU-1000 and NU-1000-Rh. (C) The pore size distribution of NU-1000 and NU-1000-Rh obtained using DFT calculations.

and the pore size is reduced from 3.68 nm to 3.38 nm after Rh catalyst loading as evidenced by DFT calculation (Figure 2C).

The electrochemical response of the GC-NU1000-Rh electrodes loaded with different ratios of Rh catalyst (0%,10%, 50% and 100%) were characterized by cylic voltammetry (CV) in 50 mM Tris buffer at pH 7.2 under nitrogen. Tris buffer was chosen instead of PBS because NU-1000 is not stable in PBS buffer, as the phosphate ions coordinate with the NU-1000 framework, which has been actually used for drug release.[47] From the CV curves shown in **Figure 3A**, a peak corresponding to $[Rh(Cp^*)(bpy)Cl]^+$ reduction is observed around -0.7 V, while the oxidation signal is located around -0.62 V. The amount of electrochemically active Rh catalyst was calculated by integration of the reduction peak in the cyclic voltammograms (Table S2). Comparing these values with the Rh catalyst percentage estimated by EDS, it seems that they are following a similar trend as a function of the initial Rh catalyst ratio in the SALI solution (**Figure S4A**). We also tried to evaluate the average distance between the Rh centers for the different degrees of Rh loading based on a simplified geometric model (**Figure S4B**). The estimated distances are approximately 2nm for a sample with a nominal loading of 100%, 2.8nm for 50% and 5nm for 10%, indicating that even with the lowest loading, the redox centers are still close enough for allowing electron hopping.

However, the efficiency of the redox hoping being a function of the distance between the redox active center, the current increases for higher ratios of Rh catalyst in the NU-1000 film, and the electrode modified with 100% Rh-COOH (GC-NU1000-Rh) shows the highest redox signal.

Then, the electrocatalytic responses of GC-NU1000-Rh (0%, 10%, 50% and 100%) towards NAD^+ reduction was measured. **Figure 3B** depicts the evolution of the response of a GC-NU1000-Rh electrode, and a linear increase of cathodic catalytic current was observed for

successive additions of NAD^+ to the solution. The same experiments were also conducted with the electrodes functionalized with 0%, 10%, and 50% Rh catalyst (corresponding CVs are shown in **Figure S5).** Their CV response to the addition of 0.2 mM NAD^+ is shown in **Figure 3C**, and their catalytic currents at -0.72 V as a function of NAD^+ concentration are shown in **Figure 3D**, indicating that the electrocatalytic performance towards NADH regeneration can be fine-tuned by a precise control the Rh catalyst loading. The resulting catalytic current density (16 $\mu A/cm^2$) is improved by up to two orders of magnitude compared to the value reported for a Rh catalyst functionalized on a CNTs-carbon felt electrode (0.11 $\mu A/cm^2$),[11] indicating a much higher grafting density of the Rh catalyst per unit of active surface area on the GC-NU1000-Rh electrode and an efficient redox hoping throughout the MOF layer.[48,49]

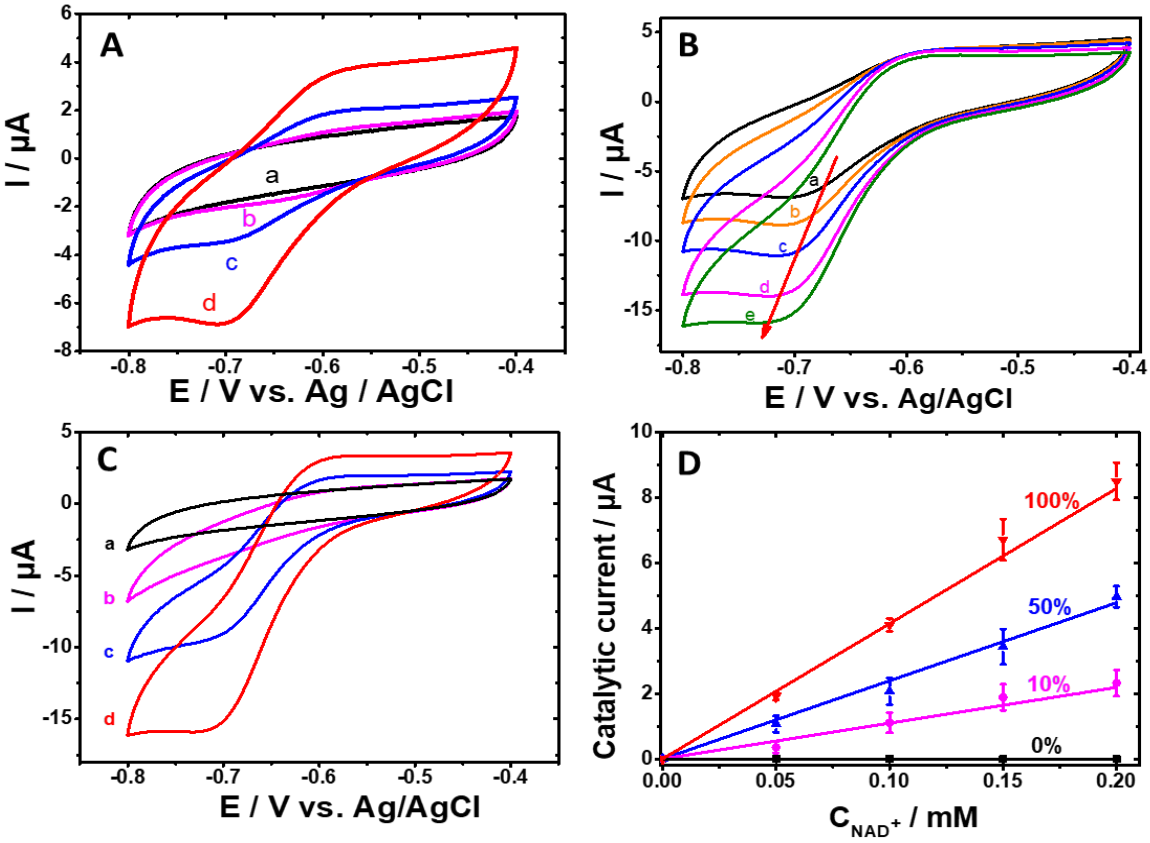

Figure 3. (A) Cyclic voltammograms recorded with GC-NU1000-Rh electrodes with different ratios of Rh catalyst (a) 0%, (b) 10%, (c) 50%, and (d) 100%. (B) Cyclic voltammograms recorded with a GC-NU1000-Rh (100%) electrode after the addition of (a) 0 mM, (b) 0.05 mM, (c) 0.10 mM, (d) 0.15 mM, and (e) 0.20 mM NAD^+. Experiments are carried out in 50 mM Tris buffer (pH 7.2) at the scan rate of 5 $mV \cdot s^{-1}$ under nitrogen. The surface area of the electrode is 1 cm^2. (C) Cyclic voltammograms of GC-NU1000-Rh (0%, 10%, 50% and 100%) electrodes in the presence of 0.2 mM NAD^+. (D) Plot of catalytic current as a function of NAD^+ concentration for GC-NU1000-Rh electrodes with different ratios of Rh catalyst. The catalytic currents have been corrected by subtracting the background current measured in the absence of NAD^+. Error bars refer to three measurements with different samples.

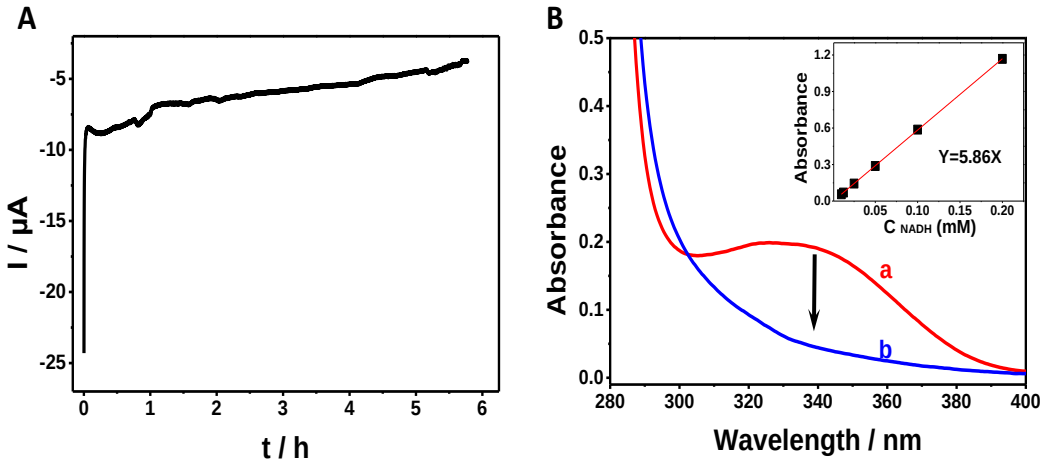

Figure 4. (A) Amperometric response recorded with a GC-NU-1000-Rh electrode in 0.5 mM NAD^+ at an applied potential of -0.72 V for 5.8 h in 30 mL Tris buffer (pH 7.2). (B) UV/Vis absorption spectra of the electrosynthesis product obtained before (a) and after (b) the addition of 100 U alcohol dehydrogenase and 50 mM acetaldehyde. The inset shows the calibration curve of NADH based on the absorbance at a wavelength of 340 nm.

After having confirmed the tunable catalytic activity of such electrodes, another important aspect is to examine the possibility to use them for the quantitative regeneration of NADH. Long-term experiments were therefore carried out with a GC-NU1000-Rh electrode, biased at a potential of −0.72 V in the presence of 0.5 mM NAD^+ under stirring (**Figure 4A**). After 5.8 h of electrolysis, UV-vis spectra were used to characterize the produced 1,4-NADH, based on its intrinsic absorption peak at 340 nm. In order to make sure that the product is enzymatically active 1,4-NADH, and not some parasitic by-product, NAD-dependent alcohol dehydrogenase and acetaldehyde substrate were added to the solution, following a reported protocol[10]. The amount of produced 1,4-NADH was calculated from the decrease of the absorption at 340 nm (**Figure 4B**), based on a previously recorded calibration curve (inset in **Figure 4B**). These measurements we also used to study a potential leaching of the catalyst. Since the Rh catalyst has a typical absorption peak at 299 nm, 310 nm and 380 nm,[11] and we didn't observe an specific absorption signals at these wavelengths in the reaction product solution after long-term

electrolysis, it is reasonable to assume that there is no leakage of Rh catalyst into the solution. This was further confirmed by electrochemical measurements. The amount of electrochemically active Rh catalyst was calculated from the CVs, recorded before and after the electrocatalysis experiments. It decreases from 7.76×10^{-11} to $7.41\text{x}10^{-11}$ mol, which corresponds to a loss of only 4%, indicating that there is no significant leaking of the incorporated Rh catalyst (**Figure S6**).

The amount of produced 1,4-NADH was estimated to be $6.36\text{x}10^{-7}$ mol, corresponding to a Faradaic efficiency of 97%. The amount of electroactive $[Rh(Cp^*)(bpy)Cl]^+$ on the electrode was estimated to be 7.76×10^{-11} mol by integrating the reduction peak of the CV. Thus, the turnover frequency (TOF) for NADH can be estimated to be ~1400 h^{-1}. Even though being lower than what can be achieved with an enzyme-based electroregeneration associated to surface immobilization[51], it is nevertheless a high value for electrocatalytic NADH regeneration, compared to what has been reported so far in the literature for immobilized Rh complexes (3.6~1100 h^{-1}).[11,52] This high efficiency can be ascribed to the precise loading and the homogeneous distribution of $[Rh(Cp^*)(bpy)Cl]^+$ in the 3D framework, with a well-defined distance between each catalytic site (~2 nm estimated from the structure of NU-1000), ensuring that each catalyst unit experiences a similar microenvironment, which can efficiently take part in NADH regeneration.

Finally, the GC-NU1000-Rh electrode was used for electroenzymatic synthesis, and L-lactate dehydrogenase (LDH) has been chosen as a model enzyme for the conversion of pyruvate into L-lactate. The size of LDH is reported to be $6\times8.6\times13.6$ nm,[53] and the pore size of NU1000-Rh is around 3.4 nm, thus LDH is not able to diffuse into the pores, but the small-sized NADH molecules ($1.3\times1.1\times1.9$ nm)[24] can shuttle electrons between the Rh catalyst in the NU1000 film and LDH in the solution. In a chronoamperometry experiment with the GC-NU1000-Rh electrode biased at -0.72 V, in the presence of 0.1 mM NAD^+ and 200 U LDH, 1.63×10^{-6} mol

pyruvate has been quantitatively converted into L-lactate after 9 h electrolysis, as characterized by HPLC (**Figure S7**). This corresponds to a TTN of ~21000 for the immobilized $[Cp^*Rh(bpy)Cl]^+$ catalyst, whereas the highest TTN in the literature has been reported to be 12000 after reacting for 95h with an immobilized Rh catalyst[9]. Thus, such a rather high value allows envisioning interesting applications in the frame of enzyme driven bioconversion.

CONCLUSION

We propose an original and highly efficient electrocatalytic system for NADH cofactor regeneration based on NU-1000 films immobilized on glassy carbon electrodes. An electrochemically grafted carboxyphenyl layer acts as an adhesion layer for the generated MOF films and helps controlling the density and orientation of the crystalline rods. The $[Rh(Cp^*)(bpy)Cl]^+$ catalyst can be successfully immobilized at the Zr_6 nodes of the film via the SALI process. A precise loading of the catalyst is achieved by tuning the molar ratio between Rh catalyst and redox inactive species. The resulting electrocatalytic response towards NADH regeneration has been shown to be directly proportional to the amount of catalyst. The films with a maximum loading of Rh catalyst, corresponding to a final molar ratio of 0.9:1 with respect to the Zr_6 nodes, exhibit the highest electrocatalytic currents. Electrochemical bulk transformation experiments from NAD^+ to NADH reveal a very high TOF of ~1400 h^{-1} and an exceptionally high Faradaic efficiency of 97%, combined with an electroenzymatic conversion of pyruvate into L-lactate with a TTN of over 20000 when using L-Lactate dehydrogenase as a model enzyme. This makes the proposed catalytic system very attractive for electroenzymatic synthesis, and also opens up interesting perspectives for generalizing the concept with other catalysts used in electroorganic synthesis.

ASSOCIATED CONTENT

Supporting Information.

Supplementary calculations of faradic efficiency and turnover frequency (TOF) for NADH regeneration and L-lactate production; Supplementary figures including cyclic voltammograms for different electrodes, optical pictures of the control electrode, atomic percentage measured from EDS, as well as calibration curves and HPLC measurements.

Corresponding Author

* lin.zhang@henu.edu.cn; *kuhn@enscbp.fr

Author Contributions

The manuscript was written through contributions of all authors. All authors have given approval to the final version of the manuscript. ‡ Weiwei Li and Chunhua Zhang contributed equally to this work.

Notes

The authors declare no competing financial interest.

ACKNOWLEDGMENT

The work has been funded by the National Natural Science Foundation of China (No. 21902045) and Henan center for Outstanding Overseas Scientist (GZS2020005). The project has also been supported by the European Research Council (ERC) under the European Union's Horizon 2020 research and innovation program (grant agreement no 741251, ERC Advanced grant ELECTRA).

REFERENCES

(1) Simon, E.; Bartlett, P. N. *Biomolecular Films: Design, Function,and Applications*; Rusling, J. F., Ed.; CRC Press, 2003.

(2) Liu, W.; Hu, W.; Yang, L.; Liu, J. Single Cobalt Atom Anchored on Carbon Nitride with Well-Defined Active Sites for Photo-Enzyme Catalysis. *Nano Energy* **2020**, *73* (April), 104750. https://doi.org/10.1016/j.nanoen.2020.104750.

(3) Zhang, Y.; Liu, J. Bioinspired Photocatalytic NADH Regeneration by Covalently Metalated Carbon Nitride for Enhanced CO_2 Reduction. *Chem. Eur. J.* **2022**, e2001430.

(4) Lee, Y. S.; Gerulskis, R.; Minteer, S. D. Advances in Electrochemical Cofactor Regeneration: Enzymatic and Non-Enzymatic Approaches. *Curr. Opin. Biotechnol.* **2022**, *73*, 14–21. https://doi.org/10.1016/j.copbio.2021.06.013.

(5) Gorton, L.; Dominguez, E. Electrochemistry of $NAD(P)^+$/NAD(P)H. In *Encyclopedia of Electrochemistry*; 2002; Vol. 9, pp 67–143. https://doi.org/10.1002/9783527610426.bard090004.

(6) Walcarius, A.; Nasraoui, R.; Wang, Z.; Qu, F.; Urbanova, V.; Etienne, M.; Göllü, M.; Demir, A. S.; Gajdzik, J.; Hempelmann, R. Factors Affecting the Electrochemical Regeneration of NADH by (2,2'-Bipyridyl) (Pentamethylcyclopentadienyl)-Rhodium Complexes: Impact on Their Immobilization onto Electrode Surfaces. *Bioelectrochemistry* **2011**, *82* (1), 46–54. https://doi.org/10.1016/j.bioelechem.2011.05.002.

(7) Hildebrand, F.; Lütz, S. Stable Electroenzymatic Processes by Catalyst Separation. *Chem. Eur. J.* **2009**, *15*, 4998–5001. https://doi.org/10.1002/chem.200900219.

(8) Tan, B.; Hickey, D. P.; Milton, R. D.; Giroud, F.; Minteer, S. D. Regeneration of the NADH Cofactor by a Rhodium Complex Immobilized on Multi-Walled Carbon Nanotubes. *J. Electrochem. Soc.* **2015**, *162* (3), H102–H107. https://doi.org/10.1149/2.0111503jes.

(9) Zhang, L.; Etienne, M.; Vilà, N.; Le, T. X. H.; Kohring, G. W.; Walcarius, A. Electrocatalytic Biosynthesis Using a Bucky Paper Functionalized by $[Cp^*Rh(Bpy)Cl]^+$and a Renewable Enzymatic Layer. *ChemCatChem* **2018**, *10* (18), 4067–4073. https://doi.org/10.1002/cctc.201800681.

(10) Zhang, C.; Zhang, H.; Pi, J.; Zhang, L.; Kuhn, A. Bulk Electrocatalytic NADH Cofactor Regeneration with Bipolar Electrochemistry. *Angew. Chem. Int. Ed.* **2022**, *61*, e202111804. https://doi.org/10.1002/anie.202111804.

(11) Zhang, L.; Vilà, N.; Kohring, G. W.; Walcarius, A.; Etienne, M. Covalent Immobilization of (2,2′-Bipyridyl) (Pentamethylcyclopentadienyl)-Rhodium Complex on a Porous Carbon Electrode for Efficient Electrocatalytic NADH Regeneration. *ACS Catal.* **2017**, *7* (7), 4386–4394. https://doi.org/10.1021/acscatal.7b00128.

(12) Zhang, L.; Vilà, N.; Walcarius, A.; Etienne, M. Molecular and Biological Catalysts Coimmobilization on Electrode by Combining Diazonium Electrografting and Sequential Click Chemistry. *ChemElectroChem* **2018**, *5* (16), 2208–2217. https://doi.org/10.1002/celc.201800258.

(13) Lin, G.; Zhang, Y.; Hua, Y.; Zhang, C.; Jia, C.; Ju, D.; Yu, C.; Li, P.; Liu, J. Bioinspired Metalation of the Metal-Organic Framework MIL-125-NH_2 for Photocatalytic NADH Regeneration and Gas-Liquid-Solid Three-Phase Enzymatic CO_2 Reduction. *Angew. Chemie - Int. Ed.* **2022**. https://doi.org/10.1002/anie.202206283.

(14) Xia, H.; Li, Z.; Zhong, X.; Li, B.; Jiang, Y.; Jiang, Y. HKUST-1 Catalyzed Efficient in Situ Regeneration of NAD^+ for Dehydrogenase Mediated Oxidation. *Chem. Eng. Sci.* **2019**, *203*, 43–53. https://doi.org/10.1016/j.ces.2019.03.076.

(15) Al-Kutubi, H.; Gascon, J.; Sudhölter, E. J. R.; Rassaei, L. Electrosynthesis of Metal-Organic Frameworks: Challenges and Opportunities. *ChemElectroChem* **2015**, *2* (4), 462–474. https://doi.org/10.1002/celc.201402429.

(16) Yadnum, S.; Roche, J.; Lebraud, E.; Négrier, P.; Garrigue, P.; Bradshaw, D.; Warakulwit, C.; Limtrakul, J.; Kuhn, A. Site-Selective Synthesis of Janus-Type Metal-Organic Framework Composites. *Angew. Chemie - Int. Ed.* **2014**, *53* (15), 4001–4005. https://doi.org/10.1002/anie.201400581.

(17) Suttipat, D.; Butcha, S.; Assavapanumat, S.; Maihom, T.; Gupta, B.; Perro, A.; Sojic, N.; Kuhn, A.; Wattanakit, C. Chiral Macroporous MOF Surfaces for Electroassisted Enantioselective Adsorption and Separation. *ACS Appl. Mater. Interfaces* **2020**, *12* (32), 36548–36557. https://doi.org/10.1021/acsami.0c09816.

(18) Warakulwit, C.; Yadnum, S.; Boonyuen, C.; Wattanakit, C.; Karajic, A.; Garrigue, P.; Mano, N.; Bradshaw, D.; Limtrakul, J.; Kuhn, A. Elaboration of Metal Organic Framework Hybrid Materials with Hierarchical Porosity by Electrochemical Deposition-

Dissolution. *CrystEngComm* **2016**, *18* (27), 5095–5100. https://doi.org/10.1039/c6ce00658b.

(19) Xie, L. S.; Skorupskii, G.; Dincă, M. Electrically Conductive Metal-Organic Frameworks. *Chem. Rev.* **2020**, *120* (16), 8536–8580. https://doi.org/10.1021/acs.chemrev.9b00766.

(20) Wang, T. C.; Vermeulen, N. A.; Kim, I. S.; Martinson, A. B. F.; Fraser Stoddart, J.; Hupp, J. T.; Farha, O. K. Scalable Synthesis and Post-Modification of a Mesoporous Metal-Organic Framework Called NU-1000. *Nat. Protoc.* **2016**, *11* (1), 149–162. https://doi.org/10.1038/nprot.2016.001.

(21) de Ruiter, M. V.; Mejia-Ariza, R.; Cornelissen, J. J. L. M.; Huskens, J. Hierarchical Pore Structures as Highways for Enzymes and Substrates. *Chem* **2016**, *1* (1), 29–31. https://doi.org/10.1016/j.chempr.2016.06.009.

(22) Chen, Y.; Jiḿenez-Ángeles, F.; Qiao, B.; Krzyaniak, M. D.; Sha, F.; Kato, S.; Gong, X.; Buru, C. T.; Chen, Z.; Zhang, X.; Gianneschi, N. C.; Wasielewski, M. R.; De La Cruz, M. O.; Farha, O. K. Insights into the Enhanced Catalytic Activity of Cytochrome c When Encapsulated in a Metal-Organic Framework. *J. Am. Chem. Soc.* **2020**, *142* (43), 18576–18582. https://doi.org/10.1021/jacs.0c07870.

(23) Sha, F.; Chen, Y.; Drout, R. J.; Idrees, K. B.; Zhang, X.; Farha, O. K. Stabilization of an Enzyme Cytochrome c in a Metal-Organic Framework against Denaturing Organic Solvents. *iScience* **2021**, *24* (6), 102641. https://doi.org/10.1016/j.isci.2021.102641.

(24) Chen, Y.; Li, P.; Noh, H.; Kung, C. W.; Buru, C. T.; Wang, X.; Zhang, X.; Farha, O. K. Stabilization of Formate Dehydrogenase in a Metal–Organic Framework for

Bioelectrocatalytic Reduction of CO_2. *Angew. Chemie. Int. Ed.* **2019**, *58* (23), 7682–7686. https://doi.org/10.1002/anie.201901981.

(25) Chuang, C. H.; Kung, C. W. Metal−Organic Frameworks toward Electrochemical Sensors: Challenges and Opportunities. *Electroanalysis* **2020**, *32* (9), 1885–1895. https://doi.org/10.1002/elan.202060111.

(26) Biswas, S.; Chen, Y.; Xie, Y.; Sun, X.; Wang, Y. Polypyrrole Merged Zirconium-Based Metal-Organic Framework NU-1000 for Detection of Levodopa. *Microchim. Acta* **2020**, *187* (12). https://doi.org/10.1007/s00604-020-04622-y.

(27) Sanati, S.; Abazari, R.; Morsali, A. Enhanced Electrochemical Oxygen and Hydrogen Evolution Reactions Using an NU-1000@NiMn-LDHS Composite Electrode in Alkaline Electrolyte. *Chem. Commun.* **2020**, *56* (49), 6652–6655. https://doi.org/10.1039/d0cc01146k.

(28) Noh, H.; Kung, C. W.; Otake, K. I.; Peters, A. W.; Li, Z.; Liao, Y.; Gong, X.; Farha, O. K.; Hupp, J. T. Redox-Mediator-Assisted Electrocatalytic Hydrogen Evolution from Water by a Molybdenum Sulfide-Functionalized Metal-Organic Framework. *ACS Catal.* **2018**, *8* (10), 9848–9858. https://doi.org/10.1021/acscatal.8b02921.

(29) Liu, B.; Thoi, V. S. Improving Charge Transfer in Metal-Organic Frameworks through Open Site Functionalization and Porosity Selection for Li-S Batteries. *Chem. Mater.* **2020**, *32* (19), 8450–8459. https://doi.org/10.1021/acs.chemmater.0c02438.

(30) Talin, A. A.; Centrone, A.; Ford, A. C.; Foster, M. E.; Stavila, V.; Haney, P.; Kinney, R. A.; Szalai, V.; El Gabaly, F.; Yoon, H. P.; Léonard, F.; Allendorf, M. D. Tunable

Electrical Conductivity in Metal-Organic Framework Thin-Film Devices. *Science* **2014**, *343* (6166), 66–69. https://doi.org/10.1126/science.1246738.

(31) Goswami, S.; Ray, D.; Otake, K. I.; Kung, C. W.; Garibay, S. J.; Islamoglu, T.; Atilgan, A.; Cui, Y.; Cramer, C. J.; Farha, O. K.; Hupp, J. T. A Porous, Electrically Conductive Hexa-Zirconium(Iv) Metal-Organic Framework. *Chem. Sci.* **2018**, *9* (19), 4477–4482. https://doi.org/10.1039/c8sc00961a.

(32) Wang, T. C.; Hod, I.; Audu, C. O.; Vermeulen, N. A.; Nguyen, S. T.; Farha, O. K.; Hupp, J. T. Rendering High Surface Area, Mesoporous Metal-Organic Frameworks Electronically Conductive. *ACS Appl. Mater. Interfaces* **2017**, *9* (14), 12584–12591. https://doi.org/10.1021/acsami.6b16834.

(33) Shimoni, R.; He, W.; Liberman, I.; Hod, I. Tuning of Redox Conductivity and Electrocatalytic Activity in Metal-Organic Framework Films Via Control of Defect Site Density. *J. Phys. Chem. C* **2019**, *123* (9), 5531–5539. https://doi.org/10.1021/acs.jpcc.8b12392.

(34) Lin, S.; Usov, P. M.; Morris, A. J. The Role of Redox Hopping in Metal-Organic Framework Electrocatalysis. *Chem. Commun.* **2018**, *54* (51), 6965–6974. https://doi.org/10.1039/c8cc01664j.

(35) Ahrenholtz, S. R.; Epley, C. C.; Morris, A. J. Solvothermal Preparation of an Electrocatalytic Metalloporphyrin MOF Thin Film and Its Redox Hopping Charge-Transfer Mechanism. *J. Am. Chem. Soc.* **2014**, *136* (6), 2464–2472. https://doi.org/10.1021/ja410684q.

(36) Hod, I.; Farha, O. K.; Hupp, J. T. Modulating the Rate of Charge Transport in a Metal-Organic Framework Thin Film Using Host:Guest Chemistry. *Chem. Commun.* **2016**, *52* (8), 1705–1708. https://doi.org/10.1039/c5cc09695b.

(37) Goswami, S.; Hod, I.; Duan, J. D.; Kung, C. W.; Rimoldi, M.; Malliakas, C. D.; Palmer, R. H.; Farha, O. K.; Hupp, J. T. Anisotropic Redox Conductivity within a Metal-Organic Framework Material. *J. Am. Chem. Soc.* **2019**, *141* (44), 17696–17702. https://doi.org/10.1021/jacs.9b07658.

(38) Van Gough, D.; Lambert, T. N.; Wheeler, D. R.; Rodriguez, M. A.; Brumbach, M. T.; Allendorf, M. D.; Spoerke, E. D. Controlled Nucleation and Growth of Pillared Paddlewheel Framework Nanostacks onto Chemically Modified Surfaces. *ACS Appl. Mater. Interfaces* **2014**, *6* (3), 1509–1514. https://doi.org/10.1021/am404102f.

(39) Hermes, S.; Schröder, F.; Chelmowski, R.; Wöll, C.; Fischer, R. A. Selective Nucleation and Growth of Metal-Organic Open Framework Thin Films on Patterned COOH/CF3-Terminated Self-Assembled Monolayers on Au(111). *J. Am. Chem. Soc.* **2005**, *127* (40), 13744–13745. https://doi.org/10.1021/ja053523l.

(40) Biemmi, E.; Scherb, C.; Bein, T. Oriented Growth of the Metal Organic Framework $Cu_3(BTC)_2(H_2O)_3 \cdot xH_2O$ Tunable with Functionalized Self-Assembled Monolayers. *J. Am. Chem. Soc.* **2007**, *129* (26), 8054–8055. https://doi.org/10.1021/ja0701208.

(41) Verma, P. K.; Huelsenbeck, L.; Nichols, A. W.; Islamoglu, T.; Heinrich, H.; Machan, C. W.; Giri, G. Controlling Polymorphism and Orientation of NU-901/NU-1000 Metal-Organic Framework Thin Films. *Chem. Mater.* **2020**, *32* (24), 10556–10565. https://doi.org/10.1021/acs.chemmater.0c03539.

(42) Chuang, C. H.; Li, J. H.; Chen, Y. C.; Wang, Y. Sen; Kung, C. W. Redox-Hopping and Electrochemical Behaviors of Metal−organic Framework Thin Films Fabricated by Various Approaches. *J. Phys. Chem. C* **2020**, *124* (38), 20854–20863. https://doi.org/10.1021/acs.jpcc.0c03873.

(43) Phal, S.; Shimizu, K.; Mwanza, D.; Mashazi, P.; Shchukarev, A.; Tesfalidet, S. Electrografting of 4-Carboxybenzenediazonium on Glassy Carbon Electrode: The Effect of Concentration on the Formation of Mono and Multilayers. *Molecules* **2020**, *25* (19), 1–12. https://doi.org/10.3390/molecules25194575.

(44) Webber, T. E.; Liu, W. G.; Desai, S. P.; Lu, C. C.; Truhlar, D. G.; Penn, R. L. Role of a Modulator in the Synthesis of Phase-Pure NU-1000. *ACS Appl. Mater. Interfaces* **2017**, *9* (45), 39342–39346. https://doi.org/10.1021/acsami.7b11348.

(45) Deria, P.; Bury, W.; Hupp, J. T.; Farha, O. K. Versatile Functionalization of the Nu-1000 Platform by Solvent-Assisted Ligand Incorporation. *Chem. Commun.* **2014**, *50* (16), 1965–1968. https://doi.org/10.1039/c3cc48562e.

(46) Cai, M.; Loague, Q.; Morris, A. J. Design Rules for Efficient Charge Transfer in Metal-Organic Framework Films: The Pore Size Effect. *J. Phys. Chem. Lett.* **2020**, *11* (3), 702–709. https://doi.org/10.1021/acs.jpclett.9b03285.

(47) Chen, Y.; Li, P.; Modica, J. A.; Drout, R. J.; Farha, O. K. Acid-Resistant Mesoporous Metal-Organic Framework toward Oral Insulin Delivery: Protein Encapsulation, Protection, and Release. *J. Am. Chem. Soc.* **2018**, *140* (17), 5678–5681. https://doi.org/10.1021/jacs.8b02089.

(48) Shen, C. H.; Chuang, C. H.; Gu, Y. J.; Ho, W. H.; Song, Y. Da; Chen, Y. C.; Wang, Y. C.; Kung, C. W. Cerium-Based Metal-Organic Framework Nanocrystals Interconnected by Carbon Nanotubes for Boosting Electrochemical Capacitor Performance. *ACS Appl. Mater. Interfaces* **2021**, *13* (14), 16418–16426. https://doi.org/10.1021/acsami.1c02038.

(49) Usov, P. M.; Huffman, B.; Epley, C. C.; Kessinger, M. C.; Zhu, J.; Maza, W. A.; Morris, A. J. Study of Electrocatalytic Properties of Metal-Organic Framework PCN-223 for the Oxygen Reduction Reaction. *ACS Appl. Mater. Interfaces* **2017**, *9* (39), 33539–33543. https://doi.org/10.1021/acsami.7b01547.

(50) Yuan, M.; Kummer, M. J.; Milton, R. D.; Quah, T.; Minteer, S. D. Efficient NADH Regeneration by a Redox Polymer-Immobilized Enzymatic System. *ACS Catal.* **2019**, *9*, 5486–5495. https://doi.org/10.1021/acscatal.9b00513.

(51) Ganesan, V.; Sivanesan, D.; Yoon, S. Correlation between the Structure and Catalytic Activity of [Cp*Rh(Substituted Bipyridine)] Complexes for NADH Regeneration. *Inorg. Chem.* **2017**, *56* (3), 1366–1374. https://doi.org/10.1021/acs.inorgchem.6b02474.

(52) Ei-Zahab, B.; Jia, H.; Wang, P. Enabling Multienzyme Biocatalysis Using Nanoporous Materials. *Biotechnol. Bioeng.* **2004**, *87* (2), 178–183. https://doi.org/10.1002/bit.20131.

(53) Mondloch, J. E.; Bury, W.; Fairen-Jimenez, D.; Kwon, S.; Demarco, E. J.; Weston, M. H.; Sarjeant, A. A.; Nguyen, S. T.; Stair, P. C.; Snurr, R. Q.; Farha, O. K.; Hupp, J. T. Vapor-Phase Metalation by Atomic Layer Deposition in a Metal-Organic Framework. *J. Am. Chem. Soc.* **2013**, *135* (28), 10294–10297. https://doi.org/10.1021/ja4050828.

TOC Figure